Research Square

Preprints are preliminary reports that have not undergone peer review.
They should not be considered conclusive, used to inform clinical practice,
or referenced by the media as validated information.

Sea spray may suppress wintertime lightning activity over the Eastern Mediterranean Sea

Mustafa Asfur

mustafaa@ruppin.ac.il

Ruppin Academic Center

Jacob Silverman

National Institute of Oceanography (IOLR)

Article

Keywords: Sea-spray flux, Lightning superbolts, Eastern Mediterranean Sea, Marine boundary layer, Winter thunderstorms, Ocean–atmosphere electrical coupling

Posted Date: May 14th, 2026

DOI: https://doi.org/10.21203/rs.3.rs-8814792/v1

License: This work is licensed under a Creative Commons Attribution 4.0 International License.
Read Full License

Additional Declarations: No competing interests reported.

Abstract

Wintertime thunderstorms over the Eastern Mediterranean Sea exhibit relatively low flash rates but an anomalously high incidence of very intense cloud-to-ground (CG) discharges. Recent work suggests that sea-spray flux (SSF) may influence lightning via microphysical pathways, but its electrical effects in low-CAPE winter regimes remain poorly constrained. Here we investigate how SSF and sea state modulate lightning activity in the Israeli Mediterranean Exclusive Economic Zone (IMEEZ) during the winters of 2017–2024. We combine Earth Networks Total Lightning Network (ENTLN) observations with reanalysis-based winds, measured significant wave height, and parameterized SSF to quantify the dependence of CG density, polarity, and peak current on sea state and distance from the coast. Lightning density peaks in a narrow coastal zone and declines rapidly offshore, while mean peak current increases with both distance from shore and increasing SSF. Under high sea state conditions, lightning is strongly suppressed over the IMEEZ, yet the fraction of high peak-current CG discharges rises. These results support a framework in which enhanced SSF simultaneously inhibits lightning initiation and favors fewer, more intense CG discharges over the Eastern Mediterranean Sea.

Introduction

Thunderstorm electrification is widely understood to be dominated by non-inductive charging, arising from collisions between rimed ice particles (graupel) and smaller ice crystals in the presence of supercooled liquid water (Takahashi, 1978; MacGorman et al., 2008; Saunders, 2008). Aerosol-induced modifications of cloud microphysics has been shown to influence this process by altering the balance between warm-rain and mixed-phase microphysics (Khain et al., 2005; Rosenfeld et al., 2008; Tao et al., 2012; Fan et al., 2013). Continental or anthropogenic aerosols can suppress non-inductive charge separation and lightning by modifying droplet spectra, supercooled liquid water content, and graupel formation (*e.g.*, Phillips et al., 2022). In contrast, giant cloud condensation nuclei (CCN) characteristic of marine sea-salt aerosols have long been recognized to accelerate warm-rain processes and reduce mixed-phase cloud development (Rosenfeld et al., 2008). However, unless sea-salt aerosols significantly modify the altitude or rate of freezing, reduce graupel production, or deplete supercooled liquid water, their hygroscopic influence on the cloud droplet spectrum alone is unlikely to suppress charge separation meaningfully. Indeed, in many maritime environments with low background aerosol loading, empirical studies more often report aerosol-induced enhancement rather than suppression of lightning activity (Khain et al., 2005), suggesting that modest increases in CCN from sea spray tend to invigorate, rather than inhibit, convection and electrification.

More recently, Pan et al. (2022) proposed that coarse sea-spray particles may suppress lightning over tropical oceans by promoting rapid warm-rain formation that reduces the mixed-phase volume, thereby weakening non-inductive charging. However, this mechanism was identified under deep, tropical, high Convective Available Potential Energy (CAPE) conditions and was based on coarse sea-salt aerosol concentrations derived from reanalysis of boundary-layer fields. These fields represent environmental aerosol availability rather than directly observed in-cloud populations, so while the implied suppression

of mixed-phase processes is physically consistent, it is not yet directly confirmed at the cloud scale. Extrapolating this mechanism to the Eastern Mediterranean winter environment is nontrivial, because winter thunderstorms over the region typically develop under low-CAPE convective regimes (*e.g.*, Altaratz et al., 2003; Yair et al., 2010; Shalev et al., 2011). For sea spray to inhibit lightning under such conditions, it would likely need to be lofted rapidly into the mixed-phase region of the cloud (Khain et al., 2005), a requirement that appears physically implausible for most observed wintertime storms in the area.

At the same time, the Eastern Mediterranean Sea (EMS) exhibits a distinctive combination of meteorology, ocean state, and lightning characteristics. Extreme coastal weather in the EMS occurs predominantly during the winter months (November-April) and is associated with transient low-pressure systems that produce cloudy conditions, heavy precipitation, strong winds, high waves, strong currents, and intermittent thunderstorms (Perlin & Kit, 1999; Altaratz et al., 2003). Stormy periods are punctuated by intervals of nearly calm seas, implying strong temporal variability in sea state and, consequently, in sea-spray production. An analysis of Earth Networks Total Lightning Network (ENTLN) measurements over the Eastern Mediterranean Sea along the coast of Israel during the winters (October-April) of 2017–2023 found a mean lightning density of ~ 2 $km^{-2}{\cdot}yr^{-1}$, with approximately 10% more activity in the northern portion of the study domain than in the south (Silverman et al., 2025). Over the same period, the mean peak current of cloud-to-ground (CG) strikes was ~ 20 kA, with a dominant peak frequency of 4–6 kA for negative polarity CGs and three modal ranges (6–8, 16–18, and 30–32 kA) for positive polarity CGs (Silverman et al., 2025).

Although the Mediterranean Sea does not have lightning density among the global maxima for lightning flash rate, it is recognized as a hotspot for lightning superbolts (LSBs) activity (Asfur et al., 2020; Asfur et al., 2023; Asfur *et al.*, 2025; Silverman et al., 2025). LSBs are powerful CG discharges with exceptionally high peak currents, typically defined as within the upper ~ 1% of global lightning intensity and exceeding ~ 30 kA, which approximates the median or standard CG intensity (Rakov et al., 2013). Analysis of the Very Low Frequency (VLF) detection World Wide Lightning Location Network (WWLLN) record revealed that ~ 25% of globally detected LSBs during 2009–2018 occurred over the Mediterranean region, with a relatively high concentration over the Eastern Mediterranean, the Adriatic Sea, the Tyrrhenian Sea, and the northern Mediterranean coast of Algeria (Holzworth et al., 2019; Asfur et al., 2023). Furthermore, Asfur et al. (2023) suggested that climate-driven changes and anthropogenic impacts on Mediterranean seawater properties (pH, salinity, and total alkalinity) could enhance lightning intensity in the basin by up to ~ 25% by 2050. Within the Israeli Mediterranean Exclusive Economic Zone (IMEEZ), Silverman et al. (2025) reported a maximum multi-winter average CG lightning density of 54 $strikes{\cdot}km^{-2}{\cdot}yr^{-1}$ for 2017–2023, a regional mean of 1.3 $strikes{\cdot}km^{-2}{\cdot}yr^{-1}$, and ~ 30,000 total strikes during the 2018–2019 winter alone.

Against this backdrop, our preliminary analyses of wintertime lightning activity in the IMEEZ suggest that lightning occurrence diminishes as significant wave height and parameterized sea-spray flux increase, while the fraction of very high peak-current CG discharges rises under such conditions. These observations point to a potentially important, and overlooked, role of sea-spray flux (SSF) in modulating

both the frequency and intensity of lightning in maritime winter storms. Because a purely microphysical pathway involving rapid lofting of coarse sea salt to mixed-phase levels appears unlikely in the prevalent low-CAPE regime, we propose two possible mechanisms that can act in concert or separately through the marine boundary layer and the sea surface atmosphere electrical interface.

The first mechanism we propose is that enhanced SSF under high wind and high sea-state conditions alters the lower-atmospheric space-charge configuration. Increased production of sea-spray aerosols, many of which carry positive charge (Blanchard, 1963; Gathman & Hoppel, 1970), can modify the vertical distribution of charged particles and ions near the sea surface, potentially reducing the local positive space-charge density at the surface and weakening the vertical electric field required to sustain effective charge separation in clouds. The second mechanism involves modifications to the net charge of the ocean surface under intense wave breaking and extensive whitecapping and foaming. Under fair-weather conditions, the sea surface typically supports a localized positive charge in response to the downward-directed global electric circuit field (Rycroft et al., 2008). Foam layers produced by strong turbulence and wave breaking disrupt the conductive interface and introduce numerous air-water boundaries (Blanchard, 1963), while droplets generated by bubble bursting, especially film drops from foam caps, often carry net negative charge (Iribarne & Mason, 1967; Bhattacharyya et al., 2011). The accumulation of negatively charged droplets and foam at or near the interface may partially or fully reverse the induced positive surface charge, thereby altering the boundary condition for the near-surface electric field. Such changes could weaken the coupling between the positively charged ocean surface and the negatively charged cloud base and potentially inhibit the initiation or upward propagation of positive leaders from the sea surface, contributing to a reduction in lightning frequency.

At the same time, a reduction in atmospheric potential gradient at the sea surface would require a larger charge buildup in the cloud base to exceed the breakdown threshold. Consequently, the eventual lightning discharge, when it does occur, could exhibit substantially higher peak currents than typical CG strikes (*e.g.*, de Mesquita et al., 2012; Said et al., 2013; Mallick et al., 2014; Vuković et al., 2023; Chen et al., 2025a,b). This scenario offers a physically plausible link between enhanced SSF, suppressed lightning rates, and an increased relative frequency of superbolts over the ocean (Asfur et al., 2020) and is qualitatively consistent with the preliminary IMEEZ observations of fewer but more intense CG discharges at high sea states.

In this manuscript, we investigate the role of sea-spray flux in modulating wintertime lightning activity within the IMEEZ. Building on existing understanding of non-inductive charging and aerosol–cloud interactions, we focus on the statistical relationships between lightning occurrence and intensity, significant wave height, near-surface winds, and parameterized sea-spray flux during Eastern Mediterranean winter storms. Using ENTLN lightning data collocated with reanalysis- and model-based sea-state fields, we quantify how lightning density, polarity, and peak current vary with SSF and with distance from the coastline. We then interpret these observed relationships in the context of electrically active sea spray and foam, boundary-layer conductivity, and ocean–atmosphere electrical coupling, to

assess whether changes in SSF can help explain the apparent suppression of lightning frequency and concurrent enhancement of high–peak-current discharges in the IMEEZ during winter storms.

Material and Methods

Lightning data in the region of the IMEEZ (Fig. 1) for the period Dec 2017 – Dec 2024 was obtained from the Earth Networks Total Lightning Network (ENTLN, https://www.earthnetworks.com), which is a global network of 1800 VLF antennas that locates (Time, Latitude and Longitude), identifies (IntraCloud (IC), Cloud to Ground (CG) and polarity (+ or -) and quantifies the peak current (Ip in amperes) of lightning events call around the world, with a 67% detection efficiency for CG strikes (Mallick et al., 2013). In a later study it was determined that the detection efficiency achieved by ENTLN is 95–97% (Zhu et al., 2022). It should be noted that there are three VLF antennas along the Mediterranean shore of Israel that are part of ENTLN and are distributed more or less evenly between its northern and southern borders. The data obtained from ENTLN was processed and analyzed to determine the temporal and spatial distribution of CG events over the Mediterranean Sea within the IMEEZ.

Over the same sampling period, continuous measurements of significant wave height (H_s) and wave period (T_p) were measured at the seaward end of the Hadera power plant pier, which is ca. 2 km offshore. The measurements were made with an RDI Sentinel Workhorse instrument, deployed at 26 m bottom depth with a high sensitivity and frequency pressure sensor that measured the sea surface height above it for 20 minutes every hour. These measurements are performed by IOLR within the framework of the National Monitoring Program in Israeli Mediterranean coastal waters (https://isramar.ocean.org.il/isramar2009/station/HaderaRDI.aspx?id=1). Wind speed (Ws) data was measured and recorded by the Israeli Meteorological Service (https://ims.gov.il/he/data_gov) at the end of the Hadera port breakwater near its entrance every 10 minutes throughout the sampling period.

The H_s and T_p together with the W_s time series, were used to calculate *SSF* according to the following equations (1–3):

The wave number *k* for shallow water waves, in units of m^{-1}, is calculated as a function of T_p, the acceleration of gravity (*g*) and H_s

$$k = \frac{2\cdot}{T_p \bullet \sqrt{(g \bullet (26 + H_s)}}$$

1

Where, 26 m is the average bottom depth at the location of the wave gauge.

The wave slope (*s*) is calculated as a function of *k* and *Hs* –

$s = k \cdot H_s$ (2)

Finally, *SSF* in units of $m^3 \cdot m^{-2} \cdot s^{-1}$, is calculated according to the simplified Eq. 8 from Xu et al. (2021) –

$$SSF = 1.99 \cdot \sqrt{s} \cdot W_s \cdot 10^{-8}$$

3

Storm event segmentation and analysis

Storm events were identified using lightning occurrence as the primary segmentation variable. Where, lightning provides a physically meaningful storm delimiter because it directly reflects the presence and persistence of deep convection, mixed-phase microphysics, and charge-separation processes that define active storm dynamics (Williams, 1989; Saunders & Peck, 1998; MacGorman & Rust, 1998; Williams, 2001; Deierling & Petersen, 2008). Continuous 10-min resolution lightning time series were used to define storm activity periods, such that consecutive 10-min intervals containing at least one lightning detection were grouped into a single storm event. Storm boundaries were defined by sustained lightning-free intervals, such that a storm was considered terminated when lightning activity ceased for a minimum continuous gap duration of $\Delta t \geq 24$ h. All wind speed (W_s), significant wave height (H_s), and sea-spray flux (*SSF*) observations falling within the lightning-defined storm boundaries were assigned to the corresponding storm event. This segmentation approach ensures that each storm event represents a physically coherent convective-electrical system rather than arbitrary meteorological forcing windows, allowing event-scale integration of surface fluxes and forcing variables within dynamically connected storm structures.

Results

Seasonal and interannual variability of Cloud to Ground Lightning activity

During the winter seasons (October–April) of 2017–2024, a total of 248,146 Cloud to Ground (CG) or sea-surface lightning events were detected over the Israeli Mediterranean Exclusive Economic Zone (IMEEZ) by the Earth Networks Total Lightning Network (ENTLN). Of these CG events, 229,570 (92.5%) had negative polarity (CG-), while 18,576 (7.5%) CG events had positive polarity (CG+). Monthly counts of total CG, CG-, and CG+ events are summarized in Table SOM1. When aggregated across all winters, the overall CG-:CG+ ratio was 12.4, consistent with the dominance of negative polarity CG flashes reported for midlatitude winter thunderstorms (*e.g.*, Orville et al., 2011; Poelman et al., 2016). Monthly CG-:CG+ ratios exhibited substantial variability, ranging from a maximum of 59.1 in October 2018 to a minimum of 3.0 in February 2023. Importantly, all months that had CG events contained at least one CG+ event, and no instances were observed in which CG- occurred with a complete absence of CG+ activity.

CG lightning activity over the IMEEZ is strongly seasonal, with the majority of events occurring during early winter (October–December), although interannual variability is pronounced. When totals are pooled

across all years, November and December dominate the wintertime lightning budget, whereas March-April typically contribute relatively small fractions of the total CG counts (Table SOM1). However, the seasonal peak is not temporally fixed. Some winters are dominated by October-November lightning activity (*e.g.*, 2018–2019), others by December (*e.g.*, 2021), and still others by later-season contributions, including January or April (*e.g.*, 2023). While winter storm occurrence over the eastern Mediterranean exhibits strong interannual variability, lightning occurrence has only been examined in a limited synoptic context (*e.g.*, Yair et al., 2010), and the electrical characteristics of CG lightning, including polarity, have not been systematically explored in this context.

Interannual contrasts are particularly evident during the 2020–2021 winter, which stands out as an extreme season driven by exceptionally high CG activity in November (66,162 events) and December (38,648 events). Together, these two months account for 42% of all CG events detected over the IMEEZ during the entire study period, illustrating the outsized influence that a small number of highly electrified storm periods can exert on seasonal totals. A nonparametric Kruskal-Wallis test applied to monthly CG counts revealed no statistically significant differences in median CG activity between individual winters ($p = 0.434$), indicating that while interannual variability is large, it is dominated by episodic extremes rather than systematic year-to-year shifts in central tendency.

Beyond variations in total CG activity, the relative polarity composition of lightning exhibits a coherent seasonal structure. Even after excluding the October 2018 value (CG-:CG + = 59.1), which was identified as an outlier using the interquartile range (IQR) criterion, the mean monthly CG-:CG+ ratio decreases monotonically from October to January and increases again until April. Specifically, the mean monthly ratio declines from 26.3 in October to a minimum of 5.9 in January, before rising to 10.7 in April (Fig. 1a). This seasonal behaviour was defined using the geometric mean of the monthly CG-:CG+ ratios, computed as the mean of LOG_{10}(CG-/CG+) across winters for each calendar month (Fig. 1b). Uncertainty was estimated using a bootstrap resampling procedure across winters. A permutation test applied to LOG_{10}(CG-/CG+) confirms a highly significant month effect (permutation $p = 1.5 \cdot 10^{-4}$; 20,000 permutations), with approximately 50% of the variance in LOG_{10}(CG-/CG+) attributable to month-to-month differences. This indicates that the observed seasonal structure is extremely unlikely to arise from random variability alone.

To characterize the form of the seasonal cycle, a quadratic model was fit to the monthly mean LOG_{10}(CG-/CG+). The quadratic term (c) is significantly positive ($c = 0.0495$; 95% bootstrap confidence interval: 0.0326–0.0671), demonstrating a statistically robust U-shaped seasonal pattern. The inferred minimum occurs in late January or early February, which is consistent with mid-winter storm environments characterized by lower cloud-base heights, reduced convective vigor, and enhanced stratiform precipitation fractions, which have been associated with reduced CG- dominance in other midlatitude regions (Carey & Rutledge, 2003; Williams et al., 2005).

Taken together, these results indicate that CG lightning over the IMEEZ is concentrated within a relatively narrow portion of the winter season, but that both total lightning activity and polarity composition vary

substantially from year to year. The pronounced dominance of early-winter months in many seasons, contrasted with occasional winters peaking later, suggests that storm-track variability and the occurrence of a small number of highly electrified synoptic events exert strong control over seasonal lightning characteristics. Where, lightning occurrence over Israel has been shown to be strongly modulated by regional synoptic systems, with particular synoptic setups (e.g., deep Mediterranean cyclones and unstable flow patterns), favouring enhanced electrical activity (Shalev et al., 2011). The coherent seasonal evolution of the CG-:CG+ ratio further implies seasonal changes in storm microphysics and charge structure across the winter season, rather than purely stochastic variability, possibly reflecting seasonal variations in external forcing processes.

Spatial variability of Cloud to Ground Lightning activity

The spatial distribution of all CG events in the IMEEZ is presented in Fig. 2a, where it is evident that spatial density distribution is not homogenous with hotspots most likely indicating the regions of peak lightning activity during extreme storm events and their storm tracks. Nonetheless, it is fairly clear that lightning activity along the offshore southern boundary of the IMEEZ is relatively lower compared to northern regions by a factor of ~ 2.

The spatial homogeneity index (Fig. 2b) is generally high across the IMEEZ (~ 0.8–0.92), indicating that wintertime CG lightning is largely smoothly distributed rather than strongly clustered at the analysed spatial scale (~ 45X45 km^2). The highest homogeneity values (~ 0.9–0.92) occur in the central offshore IMEEZ, suggesting lightning there is controlled by large-scale synoptic forcing with weak mesoscale modulation. In contrast, lower homogeneity near the coastal margins and IMEEZ edges (~ 0.8–0.85) points to enhanced spatial structure associated with coastal processes, such as land-sea thermal contrasts, convergence zones, or interaction with coastal orography (offshore Carmel Headland in the north of Israel). Overall, the pattern implies a transition from structured, coastally influenced lightning near shore to nearly uniform offshore lightning organization, consistent with a shift from local to basin-scale atmospheric control during winter storms.

Finally, in Figs. 2c,d, the distance from shore is shown to be an important factor in determining the relative frequency of lightning for all CG events (Fig. 2c) and CG events with peak currents (PCs) greater than |±50 kA|. These distributions were tested for day-night effects on ENTLN detection efficiency and were found to be similar for both categories (Figs. S1 and S2). Thus, it can be concluded that the relative frequencies decrease with distance from shore but only moderately within 120 km and beyond the decrease is much more substantial. The weak decrease in CG relative frequency up to ~ 120 km offshore suggests that winter lightning activity is governed primarily by mesoscale–synoptic storm organization rather than direct coastal forcing, whereas the pronounced decline farther offshore reflects a transition into storm regions dominated by stratiform precipitation and reduced convective electrification, consistent with documented spatial asymmetries in eastern Mediterranean cyclones (*e.g.*, Yair et al., 2010; Shalev et al., 2011; Altaratz et al., 2014).

Winter Forcing Conditions and Sea-Spray Flux Characteristics

Table SOM2a shows that the storm-segmented winter record spans a wide range of event durations and sampling densities, from very short transients (< 1 h; only a few 10-min records) to multi-day synoptic episodes lasting > 100–200 h with hundreds to > 1000 samples (N). Storm intensity also varies substantially across events, with maxima in wind speed (Ws_max) and significant wave height (Hs_max) spanning from weak storms (Ws_max $\lesssim$ 5–8 m s^{-1}; Hs_max $\lesssim$ 0.5–1 m) to highly energetic events (Ws_max $\gtrsim$ 15–21 m s^{-1}; Hs_max $\gtrsim$ 4–6 m). This intensity spread is reflected in sea-spray production: storms with larger Ws_max and Hs_max generally exhibit higher mean SSF (Log10SSF_mean becomes less negative) and larger event-integrated SSF (SSF_int), indicating that sea-spray generation is strongly enhanced under energetic wind–wave conditions (Table SOM2a).

When these event metrics are considered alongside the process-space relationship between total storm $Log_{10}(SSF_{avg})$ and ΣSSF divided by storm duration (Fig. SOM1), the dataset reveals a tight exponential scaling between them ($\Sigma SSF = 3{,}165 \cdot e^{2.3 \cdot SSF_avg}$; $R^2 = 0.97$). This behaviour indicates that storm-to-storm differences in sea-spray production are not governed by linear accumulation, where small increases in SSF_{avg} correspond to disproportionately large increases in the duration-normalized integrated flux (ΣSSF). The most consistent interpretation is that sea-spray production during storms is intermittent and regime-dependent, with high-production intervals associated with enhanced wave breaking and whitecapping contributing strongly to ΣSSF and elevating the time-normalized integral beyond what would be expected from mean conditions alone. Together, Table SOM2a and the exponential relation demonstrate that storm duration sets the accumulation window, but storm intensity and peak dominance control production efficiency, yielding nonlinear amplification of event-scale SSF.

Interannual winter statistics of Ws, Hs measured at Hadera and the calculated SSF, during the lightning storm-segmented periods show a high degree of stability in forcing conditions for the winters of 2017–2025 (Table SOM2b). Mean storm event Ws (Ws_{avg}) vary narrowly between 4.4 and 4.9 $m \cdot s^{-1}$, while extreme storm intensities ($Ws_{(p95)}$) range from 9.0 to 10.7 $m \cdot s^{-1}$, indicating consistent storm forcing across winters. Similarly, storm event mean significant wave heights (Hs_{avg}) remain within 0.7–1.1 m, with upper-tail extremes ($Hs_{(p95)}$) between 1.7 and 2.8 m, reflecting stable storm-wave energetics across years. The mean Log_{10}-transformed SSF_{avg} is highly uniform (-7.9 to -7.7), while $Log_{10}SSF_{(p95)}$ values (-7.3 to -7.1) show limited interannual variability, indicating that variability in SSF production is dominated by episodic high-energy storm events rather than systematic shifts in storm-averaged forcing. Together, these results demonstrate a statistically stationary storm regime, with interannual variability expressed primarily through the frequency and intensity distribution of extreme events rather than changes in mean storm conditions.

Table SOM2c summarizes the monthly evolution of storm event Ws, Hs and SSF (reported as $Log_{10}SSF$) across each winter seasons of 2017–2025. Mean Ws is lowest in October–November and April (4.2 $m \cdot s^{-1}$) and increases to a mid-winter maximum in January (5.3 $m \cdot s^{-1}$), with medians following the same

pattern (3.7–3.8 $m \cdot s^{-1}$ in Oct-Nov versus 4.6 $m \cdot s^{-1}$ in Jan). Wave conditions show a stronger seasonal cycle, where monthly mean Hs rises from 0.6 m in October-November to 1.3 m in January, with the interquartile range widening substantially in January (0.5–1.9 m), consistent with more energetic and variable storm seas in mid-winter. Sea-spray production mirrors this seasonal intensification, with monthly $Log_{10}SSF_{avg}$ increasing from approximately − 7.9 in October–November to a peak of -7.7 in January (*i.e.*, higher flux) and then declining back toward − 7.9 by April. The interquartile ranges of $Log_{10}SSF$ similarly shift upward in December-March relative to October-November, indicating that the mid-winter enhancement reflects not only higher central tendency but also an increase in the frequency of high-flux storm conditions.

Discussion

Storm structure, spatial distribution seasonality, and electrical regimes

The results demonstrate that wintertime CG lightning over the IMEEZ is governed by a combination of strong seasonal organization, episodic extremes, and remarkably stationary background forcing. Lightning occurrence is concentrated in a limited portion of the winter season, with early-winter dominance in many years and episodic, highly electrified storm periods exerting a disproportionate influence on seasonal totals. At the same time, storm-segmented wind speed, wave height, and sea-spray flux (SSF) statistics show high interannual stability, indicating that the regional winter storm climate is statistically stationary and that variability in lightning activity is primarily driven by the occurrence and structure of extreme synoptic events rather than long-term changes in mean forcing. This decoupling between relatively stable mean forcing (Ws, Hs, SSF) and highly variable lightning output implies that lightning production in the eastern Mediterranean is not controlled simply by bulk meteorological intensity. Instead, it reflects nonlinear, threshold-dependent processes that link storm dynamics, microphysics, and electrical structure, consistent with the broader understanding that lightning is controlled by storm electrical organization and charge separation efficiency rather than convective strength alone (Williams, 2001; Carey & Rutledge, 2003; Saunders, 2008).

The spatial distribution of lightning relative to the coastline (Fig. 3) provides an independent constraint on this interpretation. Total NCG systematically increases toward the shoreline, with the highest counts occurring in the near-coastal zone and a gradual decline offshore. This pattern is difficult to attribute solely to synoptic-scale thermodynamic forcing, which varies more smoothly across the continental shelf. Instead, it aligns with the expected spatial gradient in sea-spray production and its electrical consequences, superimposed on a mesoscale coastal front that locally enhances low-level convergence and convective intensity. Wave breaking, whitecapping, and bubble bursting are maximized in shallow, fetch-limited coastal waters where wave steepness, surf-zone processes, and turbulence are enhanced (Monahan & O'Muircheartaigh, 1980; Fairall et al., 2009). These processes generate dense populations of charged droplets, film drops, and small ions that increase marine boundary-layer conductivity and modify

near-surface electric fields (Blanchard, 1963; Blanchard & Woodcock, 1980; Harrison & Carslaw, 2003). Because conductivity rises rapidly with aerosol and ion loading near the surface, the coastal zone, co-located with the strongest coastal-front convection, represents a region of particularly efficient electrical coupling between the ocean and the cloud base (Nicoll et al., 2014). The shoreward increase in NCG therefore likely reflects the combined influences of enhanced coastal convection and stronger electrically active sea spray: lightning remains most frequent near the coast, but its variability and efficiency are modulated by intensified boundary-layer electrical pathways created by local SSF production.

The exponential scaling between mean SSF and duration-normalized integrated SSF indicates that sea-spray production is regime-dependent (Fig. 4), dominated by intermittent high-production intervals, most likely associated with wave breaking, whitecapping, and surface foam formation. Such regimes are physically relevant for atmospheric electrical processes because breaking waves and bursting bubbles are known sources of charged droplets and ions, generating electrically active aerosols that can modify boundary-layer conductivity and near-surface electric fields (Blanchard, 1963; Blanchard & Woodcock, 1980; Harrison & Carslaw, 2003). These processes establish a direct physical pathway by which ocean surface state can influence atmospheric electricity, independent of cloud microphysics.

In a recent study, Pan et al. (2022) proposed a lightning suppression mechanism for highly convective marine thunderstorms in which sea-spray salt aerosols modify cloud droplet spectra and mixed-phase charging efficiency, thereby reducing lightning through microphysical processes operating within deep convective cores. This mechanism is fundamentally cloud-internal and aerosol–microphysical in nature. However, Pan et al. (2022) did not build explicitly on earlier studies examining the influence of sea-spray aerosols on cloud microphysics or lightning activity, and independent observational evidence for this specific pathway remains limited.

The eastern Mediterranean winter environment, however, represents a different dynamical and electrical regime. Winter storms over the IMEEZ are mainly baroclinic frontal systems featuring embedded convection, low cloud bases, widespread stratiform precipitation, and comparatively low CAPE relative to tropical and subtropical convective systems (Yair et al., 2010; Shalev et al., 2011; Altaratz et al., 2014). In this setting, lightning production is not dominated by deep, isolated convective towers but by mesoscale synoptic storm organization with mixed convective stratiform structures. Consequently, the microphysical suppression mechanism proposed by Pan et al. (2022) is unlikely to represent a primary control on lightning variability in this region.

Instead, the observations support a distinct, electrically mediated suppression mechanism operating through the marine atmospheric boundary layer. We propose that airborne electrified sea spray, surface foam, and whitecaps inhibit lightning discharge by modifying boundary-layer electrical conductivity and facilitating charge leakage from the cloud base to the ocean surface. In this conceptual model, sea spray does not act primarily through cloud microphysics, but through its role as an electrically active aerosol population that alters the vertical electric field structure and surface–atmosphere electrical coupling.

Electrified spray droplets and ions increase charge carrier density and electrical conductivity in the marine boundary layer, while foam and whitecaps expand the electrically active ocean surface, together enhancing conductive pathways for downward dissipation of cloud-base charge to the sea surface. This is consistent with classical and modern understandings of atmospheric electricity, in which conductivity profiles and boundary-layer ion populations regulate electric field strength and discharge conditions (Harrison & Carslaw, 2003; Rycroft et al., 2008; Nicoll et al., 2014).

Within this framework, lightning suppression emerges as a threshold process rather than a linear response to increasing sea spray. Importantly, this mechanism does not require suppression of in-cloud electrification itself. Charge separation may continue to occur, but cloud-to-ground discharge efficiency is reduced because electrical breakdown conditions at the surface are no longer met. In this sense, sea spray suppresses lightning not by weakening storms, but by inhibiting CG discharge pathways.

Multivariate (PCA) evidence for two storm modes

Auxiliary forcing parameters, including Convective Available Potential Energy (CAPE), Sea Surface Temperature (SST), surface air pressure gradients (∇P), and mean wind direction (Wd), were extracted from ERA5 for each storm segment. Mean ERA5 wind speeds were systematically lower than local measurements at Hadera and therefore, *in-situ* Ws was used for subsequent analyses. PCA performed on the full October-April (2017–2024) dataset reveals two dominant modes of variability (Fig. 5a,b). The first mode contrasts a thermodynamically controlled electrical-output regime, characterized by CAPE, SST, lightning counts (NCG, NCGn, NCGp), charge transfer (TPC±), and strong-discharge metrics (NCGp50, TNPC50), with a mechanically forced wave-spray regime dominated by wind speed (Ws), SSF, significant wave height (Hs), wave period (Tp), and mean surface pressure-gradient magnitude ($|\nabla P|$). Storm-direction classes overlap in the full-season PCA, with October storms occupying a transitional region reflecting mixed northerly and westerly regimes, relatively warm SSTs, and variable instability.

When October storms are excluded (Fig. 5b), the PCA geometry becomes clearer. Electrical-output variables collapse onto a single axis aligned with CAPE and SST, confirming that strong lightning events represent the upper tail of a single electrically productive storm regime rather than a distinct mode. The opposing axis is dominated by wind-wave-spray forcing variables (Ws, SSF, Hs, Tp, $|\nabla P|$). Storm direction classes separate coherently: N and NE flow regimes project toward the thermodynamic/lightning mode, while W and NW regimes project toward the wave-spray mode and away from lightning-rich conditions. Southerly and south-westerly regimes occupy intermediate positions. Crucially, NCGp and NCGp50 load strongly with the same electrical-output axis as total NCG, indicating that positive-polarity lightning is embedded within the same storm-scale electrical regime rather than representing a distinct physical mode.

A Sea-Spray Threshold and the Constraining of Lightning Variability

Following the PCA results, the SSF forcing axis (Ws-SSF-Hs-Tp-gradP) was further examined, whether it imposes a constraint on lightning activity across independent winter storm events. Scatter plots of storm-mean NCG versus mean SSF did not display a simple monotonic relationship, and the distribution suggested a change in behaviour at intermediate SSF values, with large event-to-event spread at low SSF and a more restricted range of NCG at higher SSF (Fig. 6). Because this pattern could not be adequately captured by a single linear or nonlinear regression, we adopted a threshold-based population comparison rather than a continuous curve fit. A visually determined threshold of ($t = 4 \cdot 10^{-8}\ m^3 \cdot m^{-2} \cdot s^{-1}$) was selected from the NCG-SSF distribution prior to formal testing. To focus on well-developed storms and reduce noise from marginal events, storms with NCG < 100 were excluded, yielding (n = 124) independent storms divided nearly evenly across the threshold ((n = 63) below t, (n = 61) above t).

For total NCG, the two SSF groups differed strongly in variance (Levene (p = 0.0006)) and modestly in mean (Welch (p = 0.0248)), indicating that increasing SSF primarily acts to constrain the population range of lightning outcomes rather than simply shifting average counts; high-SSF storms occupy a narrower, more organized region of electrical behaviour consistent with the SSF end of the PCA. In contrast, positive discharges (NCGp) showed only marginal variance contrast across the same threshold (Levene (p = 0.0523)) and no mean difference (Welch (p = 0.3771)), while high-current subsets (NCGn50 and NCGp50) exhibited no significant differences in either variance or mean (Levene (p > 0.4); Welch (p > 0.4)). Thus, the SSF-related threshold effect is expressed mainly in bulk lightning frequency (NCG) rather than in extreme-current events or in positive polarity alone, reinforcing the PCA inference that all lightning metrics load on a single thermodynamic electrical axis, while SSF forcing operates chiefly as a population-level constraint on how broadly that electrical regime is realized across storms.

Logistic sensitivity analysis (Nov–Feb, N = 93, NCG ≥ 100)

A complementary logistic sensitivity analysis for November-February storms (N = 93; NCG ≥ 100) examined whether exceedances of NNCG, NCGp, and NCGp50 could be predicted from storm-mean environmental variables using cross-validated log-loss. For moderate lightning extremes (NNCG ≥ 1000 and ≥ 2000), models based on wind direction (sin/cos) consistently performed best, suggesting that synoptic storm regime exerts a primary control on the probability of lightning exceedance. For rarer, more extreme events (NNCG ≥ 4000 and ≥ 6000), significant wave height (Hs) emerged as the most informative single predictor, although the small number of positive cases at these thresholds limits statistical confidence.

For thresholds based on strong positive discharges (NCGp50 ≥ 20 and ≥ 50), the most competitive models combined SSF, wind speed (Ws), and Hs, with Ws entering with a consistently negative coefficient. This implies that stronger winds, associated with enhanced sea spray production (SSF), tend to reduce the likelihood that a storm produces many extreme positive strokes. At the highest threshold (NCGp50 ≥ 100), model skill collapsed to the intercept owing to extreme data sparsity.

Taken together, the logistic results indicate that storm regime (as captured by wind direction) and bulk sea state (Ws and Hs) carry more predictive information for lightning exceedances than SSF alone when

its physical ingredients are included explicitly, consistent with the fact that SSF is itself parameterized from Ws, Hs, and Tp.

Conclusions

This study shows that wintertime cloud-to-ground lightning over the Israeli Mediterranean Exclusive Economic Zone is not governed primarily by mean storm intensity or CAPE, but by the interaction between synoptic storm dynamics and the proposed sea surface atmospheric electrical coupling mediated by sea state. Analysis of storm populations reveals that the relationship between sea-spray flux (SSF) and cloud-to-ground lightning (NCG) is strongly nonlinear and regime-dependent rather than monotonic. Visual and statistical threshold analysis indicates that above an intermediate SSF level of $4{\cdot}10^{-8}$ $m^3{\cdot}m^{-2}{\cdot}s^{-1}$, the storm-to-storm variability of total lightning becomes progressively constrained, with high-SSF storms occupying a much narrower range of NCG. This variance collapse, rather than a simple change in mean, suggests that increasing sea spray does not merely scale lightning up or down, but fundamentally alters the feasible electrical behaviour of storms. Positive polarity lightning (NCGp) shows only weak sensitivity to this threshold, and high-peak-current events (NCGp50 and NCGn50) show no systematic suppression, implying that the SSF effect operates mainly on bulk lightning frequency rather than on extreme discharge characteristics.

These patterns are inconsistent with explanations based solely on cloud thermodynamics or aerosol microphysical suppression within deep convection proposed by Pan et al. (2022). Instead, they support a boundary-layer electrical control mechanism in which enhanced wave breaking, whitecapping, and surface foam inject large fluxes of electrified sea spray into the marine atmospheric boundary layer. Increased near-surface conductivity provides efficient pathways for charge leakage from the cloud base to the ocean, weakening conditions for cloud-to-ground breakdown without necessarily reducing in-cloud electrification. In this view, sea spray does not “turn off” storms; it modifies the electrical environment in a way that limits total CG discharges while still permitting occasional strong strokes. This mechanism differs fundamentally from the cloud-internal salt-aerosol pathway proposed by Pan et al. (2022) for high-CAPE tropical systems and is more appropriate for the baroclinic, mixed convective-stratiform winter storms that dominate the eastern Mediterranean.

Multivariate PCA independently corroborates this interpretation by revealing two coherent storm modes: (1) a thermodynamic/lightning regime aligned with CAPE, SST, and all lightning metrics; (2) an opposing wind-wave-spray regime aligned with Ws, SSF, Hs, Tp, and gradP. When October storms are excluded, the separation sharpens, with N-NE flow regimes projecting toward lightning-rich conditions and W-NW regimes toward high-SSF, lightning-constrained conditions. Complementary logistic analysis for November-February storms further shows that synoptic regime (wind direction) best predicts moderate lightning exceedances, while wave height becomes most informative for the rarest NCG extremes and wind speed consistently acts to reduce the likelihood of many strong positive strokes. Together, these results demonstrate that marine lightning in the IMEEZ is regulated by a coupled system in which storm dynamics, cloud electrification, and surface electrical boundary conditions interact through sea state.

The region therefore exhibits two relevant lightning controls: (1) a microphysical aerosol-cloud regime characteristic of highly convective systems; (2) a boundary-layer electrical suppression regime that dominates baroclinic winter storms and explains the observed SSF thresholds, the limited role of CAPE, and the nonlinear response of lightning to the ocean surface.

Declarations

Acknowledgements and Funding Information

The author gratefully acknowledges the Earth Networks Total Lightning Network (ENTLN) for providing access to lightning data used in this study. The authors also thank the Israeli ministry of Energy for research funding (#218-13-207 and #220- 17-002).

This research did not receive any specific grant from funding agencies in the public, commercial, or not-for-profit sectors.

Contributions

Mustafa Asfur: Writing, review & editing, Visualization, Supervision, Software, sources, Project administration, Methodology, Investigation, Funding acquisition, Formal analysis, Conceptualization.

Jacob Silverman: Writing, review & editing, Visualization, Supervision, Software, sources, Project administration, Methodology, Investigation, Funding acquisition, Formal analysis, Conceptualization.

Competing interests

The authors declare no competing interests.

References

1. Altaratz, O., Koren, I., Remer, L. A. & Hirsch, E. Cloud invigoration by aerosols—Coupling between microphysics and dynamics. *Atmos. Res.* **140**, 38–60. https://doi.org/10.1016/j.atmosres.2014.01.009 (2014).
2. Altaratz, O., Levin, Z., Yair And, Y. & Ziv, B. Lightning activity over land and sea on the eastern coast of the Mediterranean. *Mon. Weather Rev.* **131** (9), 2060–2070. https://doi.org/10.1175/1520-0493((2003). 2003)131%3C2060:LAOLAS%3E2.0.CO;2.
3. Asfur, M., Silverman, J. & Price, C. Ocean acidification may be increasing the intensity of lightning over the oceans. *Sci. Rep.* **10** (1), 21847. https://doi.org/10.1038/s41598-020-79066-8 (2020).
4. Asfur, M., Price, C., Yair, Y. & Silverman, J. Spatial variability of lightning intensity over the Mediterranean sea correlates with seawater properties. *Sci. Rep.* **13** (1), 5834. https://doi.org/10.1038/s41598-023-33115-0 (2023).

5. Asfur, M. & Silverman, J. Reevaluating the global and temporal distributions of lightning superbolts: insights from ENTLN data (2018–2021). *Sci. Rep.* **15**, 45204. https://doi.org/10.1038/s41598-025-29669-w (2025).
6. Bhattacharyya, I., Maze, J. T., Ewing, G. E. & Jarrold, M. F. Charge separation from the bursting of bubbles on water. *J. Phys. Chem. A*. **115** (23), 5723–5728. https://doi.org/10.1021/jp102719s (2011).
7. Blanchard, D. C. Electrification of the atmosphere by particles from bubbles in the sea. *Prog. Oceanogr.* **1**, 73–202. https://doi.org/10.1016/0079-6611(63)90004-1 (1963).
8. Blanchard, D. C. & Woodcock, A. H. The production, concentration, and vertical distribution of the sea-salt aerosol. *Ann. N. Y. Acad. Sci.* **338**, 330–347. https://doi.org/10.1111/j.1749-6632.1980.tb17130.x (1980).
9. Carey, L. D. & Rutledge, S. A. Characteristics of cloud-to-ground lightning in severe and nonsevere storms over the central United States. *J. Geophys. Research: Atmos.* **108** (D15), 4483. https://doi.org/10.1029/2002JD002951 (2003).
10. Chen, L. et al. Analysis of lightning current above the strike point of side flash to the Canton Tower. *J. Geophys. Research: Atmos.* **130** (20). https://doi.org/10.1029/2025JD043912 (2025a). e2025JD043912.
11. Chen, L., Yuan, P., Jiang, R., An, T. & Deng, H. Study on the electric field and current intensity in lightning discharge channel based on the Hα broadening. *Atmos. Res.* 108310. https://doi.org/10.1016/j.atmosres.2025.108310 (2025b).
12. de Mesquita, C. R., Dias, R. N. & Visacro, S. Comparison of peak currents estimated by lightning location system and ground truth references obtained in Morro do Cachimbo station. *Atmos. Res.* **117**, 37–44. https://doi.org/10.1016/j.atmosres.2011.07.005 (2012).
13. Deierling, W. & Petersen, W. A. Total lightning activity as an indicator of updraft characteristics. *J. Geophys. Research: Atmos.* **113** (D16). https://doi.org/10.1029/2007JD009598 (2008).
14. Fairall, C. W., Banner, M. L., Peirson, W. L., Asher, W. & Morison, R. P. Investigation of the physical scaling of sea spray spume droplet production. *J. Geophys. Research: Oceans*. **114** (C10). https://doi.org/10.1029/2008JC004918 (2009).
15. Fan, J. et al. Microphysical effects determine macrophysical responses for aerosol impacts on deep convective clouds. *Proceedings of the National Academy of Sciences, 110*(48), E4581–E4590. (2013). https://doi.org/10.1073/pnas.1316830110
16. Gathman, S. G. & Hoppel, W. A. Electrification processes over lake superior. *J. Phys. Res.* **75** (6), 1041–1048. https://doi.org/10.1029/JC075i006p01041 (1970).
17. Harrison, R. G. & Carslaw, K. S. Ion–aerosol–cloud processes in the lower atmosphere. *Rev. Geophys.* **41** (3), 1012. https://doi.org/10.1029/2002RG000114 (2003).
18. Holzworth, R. H., McCarthy, M. P., Brundell, J. B., Jacobson, A. R. & Rodger, C. J. Global distribution of superbolts. *J. Geophys. Research: Atmos.* **124** (17–18), 9996–10005. https://doi.org/10.1029/2019JD030975 (2019).

19. Iribarne, J. V. & Mason, B. J. Electrification accompanying the bursting of bubbles in water and dilute aqueous solutions. *Trans. Faraday Soc.* **63**, 2234–2245. https://doi.org/10.1039/TF9676302234 (1967).
20. Khain, A. P., Rosenfeld, D. & Pokrovsky, A. Aerosol impact on the dynamics and microphysics of deep convective clouds. *Q. J. R. Meteorol. Soc.* **131** (611), 2639–2663. https://doi.org/10.1256/qj.04.62 (2005).
21. MacGorman, D. R. & Rust, W. D. *The electrical nature of storms* (Oxford University Press, 1998).
22. MacGorman, D. R. et al. TELEX the thunderstorm electrification and lightning experiment. *Bull. Am. Meteorol. Soc.* **89** (7), 997–1014. https://doi.org/10.1175/2007BAMS2352.1 (2008).
23. Mallick, S. et al. Calibration of the ENTLN against rocket-triggered lightning data. 2013 International Symposium on Lightning Protection (XII SIPDA), 39–46. https://doi.org/10.1109/SIPDA.2013.6729186Montanyà,, M. (2016). Global distribution of winter lightning: a threat to wind turbines and aircraft. Natural Hazards and Earth System Sciences, 16(6), 1465–1472. https://doi.org/10.5194/nhess-16-1465-2016 (2013).
24. Mallick, S. et al. On remote measurements of lightning return stroke peak currents. *Atmos. Res.* **135**, 306–313. https://doi.org/10.1016/j.atmosres.2012.08.008 (2014).
25. Monahan, E. C. & Muircheartaigh, I. Optimal power-law description of oceanic whitecap coverage dependence on wind speed. *J. Phys. Oceanogr.* **10** (12), 2094–2099. https://doi.org/10.1175/1520-0485((1980). 1980)010%3C2094:OPLDOO%3E2.0.CO;2.
26. Nicoll, K. A., Harrison, R. G. & Latham, J. The global atmospheric electric circuit: Recent advances and future directions. *Space Sci. Rev.* **168**, 1–38. https://doi.org/10.1007/s11214-011-9858-7 (2014).
27. Orville, R. E., Huffines, G. R., Burrows, W. R. & Cummins, K. L. The North American lightning detection network (NALDN)—Analysis of flash data: 2001–09. *Mon. Weather Rev.* **139** (5), 1305–1322. https://doi.org/10.1175/2010MWR3452.1 (2011).
28. Pan, Y., Fan, J., Zhang, R. & Li, Z. Suppression of lightning in maritime thunderstorms by sea spray aerosols. *Nat. Geosci.* **15**, 803–809. https://doi.org/10.1038/s41561-022-01022-0 (2022).
29. Perlin, A. & Kit, E. Longshore sediment transport on Mediterranean coast of Israel. Journal of waterway, port, coastal, and ocean engineering, **125**(2), 80–87. https://doi.org/10.1061/(ASCE)0733-950X (1999). (1999)125:2(80).
30. Phillips, D., Bansemer, V. T., Patade, A., Waman, D. & S., & New empirical formulation for the sublimational breakup of graupel and dendritic snow. *J. Atmos. Sci.* **79** (1), 317–336. https://doi.org/10.1175/JAS-D-20-0275.1 (2022).
31. Poelman, D. R., Schulz, W., Diendorfer, G. & Bernardi, M. The European lightning location system EUCLID–part 2: observations. *Nat. Hazards Earth Syst. Sci.* **16** (2), 607–616. https://doi.org/10.5194/nhess-16-607-2016 (2016).
32. Rakov, V. A. et al. CIGRE technical brochure on lightning parameters for engineering applications. In 2013 International Symposium on Lightning Protection (XII SIPDA) (pp. 373–377). IEEE. (2013).,

October https://doi.org/10.1109/SIPDA.2013.6729246

33. Rosenfeld, D. et al. Flood or drought: How do aerosols affect precipitation? *Science* **321** (5894), 1309–1313. https://doi.org/10.1126/science.1160606 (2008).
34. Rycroft, M. J., Harrison, R. G., Nicoll, K. A. & Mareev, E. A. An overview of Earth's global electric circuit and atmospheric conductivity. *Space Sci. Rev.* **137**, 83–105. https://doi.org/10.1007/s11214-008-9368-6 (2008).
35. Said, R. K., Cohen, M. B. & Inan, U. S. Highly intense lightning over the oceans: Estimated peak currents from global GLD360 observations. *J. Geophys. Research: Atmos.* **118** (13), 6905–6915. https://doi.org/10.1002/jgrd.50508 (2013).
36. Saunders, C. Charge Separation Mechanisms in Clouds. *Space Sci. Rev.* 137. https://doi.org/10.1007/s11214-008-9345-0 (2008).
37. Saunders, C. P. R. & Peck, S. L. Laboratory studies of the influence of the rime accretion rate on charge transfer during crystal/graupel collisions. *J. Geophys. Research: Atmos.* **103** (D12), 13949–13956. https://doi.org/10.1029/97JD02644 (1998).
38. Silverman, J., Yair, Y., Price, C. & Asfur, M. Cloud to surface lightning activity in the Eastern Mediterranean Sea in the context of marine infrastructure safety. *Geomatics Nat. Hazards Risk*. **16** (1), 2452351. https://doi.org/10.1080/19475705.2025.2452351 (2025).
39. Shalev, S., Saaroni, H., Izsak, T., Yair, Y. & Ziv, B. The spatio-temporal distribution of lightning over Israel and the neighboring area and its relation to regional synoptic systems. *Nat. Hazards Earth Syst. Sci.* **11** (8), 2125–2135. https://doi.org/10.5194/nhess-11-2125-2011 (2011).
40. Takahashi, T. Riming electrification as a charge generation mechanism in thunderstorms. *J. Atmos. Sci.* **35** (8), 1536–1548. https://doi.org/10.1175/1520-0469(1978) (1978). 035%3C1536:REAACG%3E2.0.CO;2.
41. Tao, W. K., Chen, J. P., Li, Z., Wang, C. & Zhang, C. Impact of aerosols on convective clouds and precipitation. *Reviews of Geophysics, 50*(2), RG2001. (2012). https://doi.org/10.1029/2011RG000369
42. Vuković, F. et al. Development and laboratory testing of a lightning current measurement system for wind turbines. *Electr. Power Syst. Res.* **223**, 109572. https://doi.org/10.1016/j.epsr.2023.109572 (2023).
43. Williams, E. R. The electrification of severe storms. In C. A. Doswell III (Ed.), Severe Convective Storms (pp. 527–561). American Meteorological Society. (2001). https://doi.org/10.1007/978-1-935704-06-5_16
44. Williams, E. R., Weber, M. E. & Orville, R. E. The relationship between lightning type and convective state of thunderclouds. *J. Geophys. Research: Atmos.* **94** (D11), 13213–13220. https://doi.org/10.1029/JD094iD11p13213 (1989).
45. Williams, E., Mushtak, V., Rosenfeld, D., Goodman, S. & Boccippio, D. Thermodynamic conditions favorable to superlative thunderstorm updraft, mixed phase microphysics and lightning flash rate. *Atmos. Res.* **76** (1–4), 288–306. https://doi.org/10.1016/j.atmosres.2004.11.009 (2005).

46. Xu, X., Voermans, J. J., Ma, H., Guan, C. & Babanin, A. V. A wind–wave-dependent sea spray volume flux model based on field experiments. Journal of Marine Science and Engineering, 9(11), 1168. (2021). https://www.mdpi.com/2077-1312/9/11/1168#.
47. Yair, Y. et al. Predicting the potential for lightning activity in Mediterranean storms based on the Weather Research and Forecasting (WRF) model dynamic and microphysical fields. *J. Geophys. Research: Atmos.* **115** (D4). https://doi.org/10.1029/2008JD010868 (2010).
48. Yair, Y., Shalev, S., Erlich, Z. & Ziv, B. Lightning activity in the eastern Mediterranean. *Atmos. Res.* **96** (2–3), 256–269. https://doi.org/10.1016/j.atmosres.2009.12.005 (2010).
49. Zhu, Y., Stock, M., Lapierre, J. & DiGangi, E. Upgrades of the Earth networks total lightning network in 2021. *Remote Sens.* **14** (9), 2209. https://doi.org/10.3390/rs14092209 (2022).

Figures

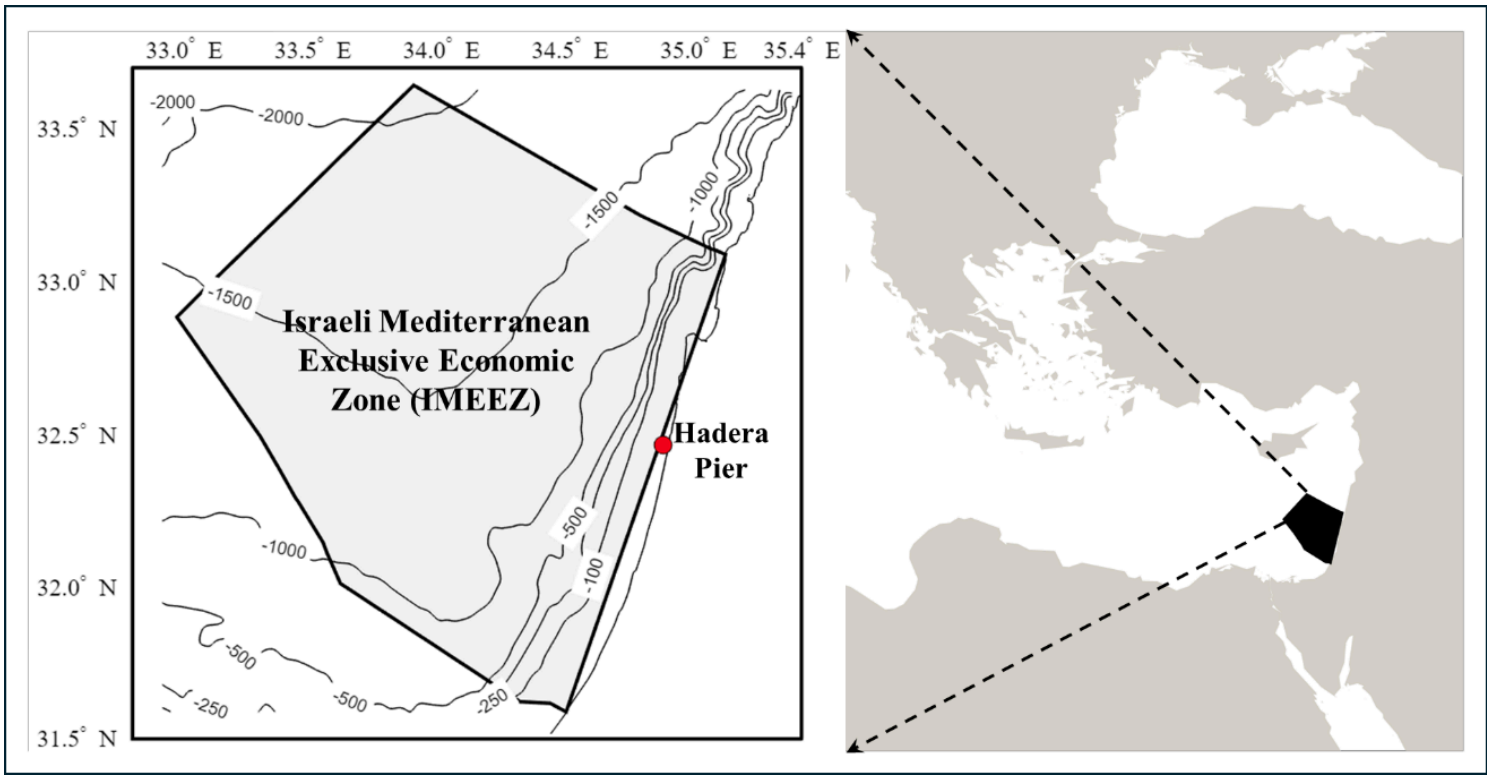


Figure 1

The Israeli Exclusive Economic Zone boundary in the Southeastern Mediterranean Sea (IMEEZ) is indicated by the black shaded polygon in the right panel. The left panel is a zoom in view of the IMEEZ including bathymetric lines (m) and the location of the Hadera Pier, where H_s and T_p were measured 2 km offshore and W_s was measured at the entrance to Hadera Port.

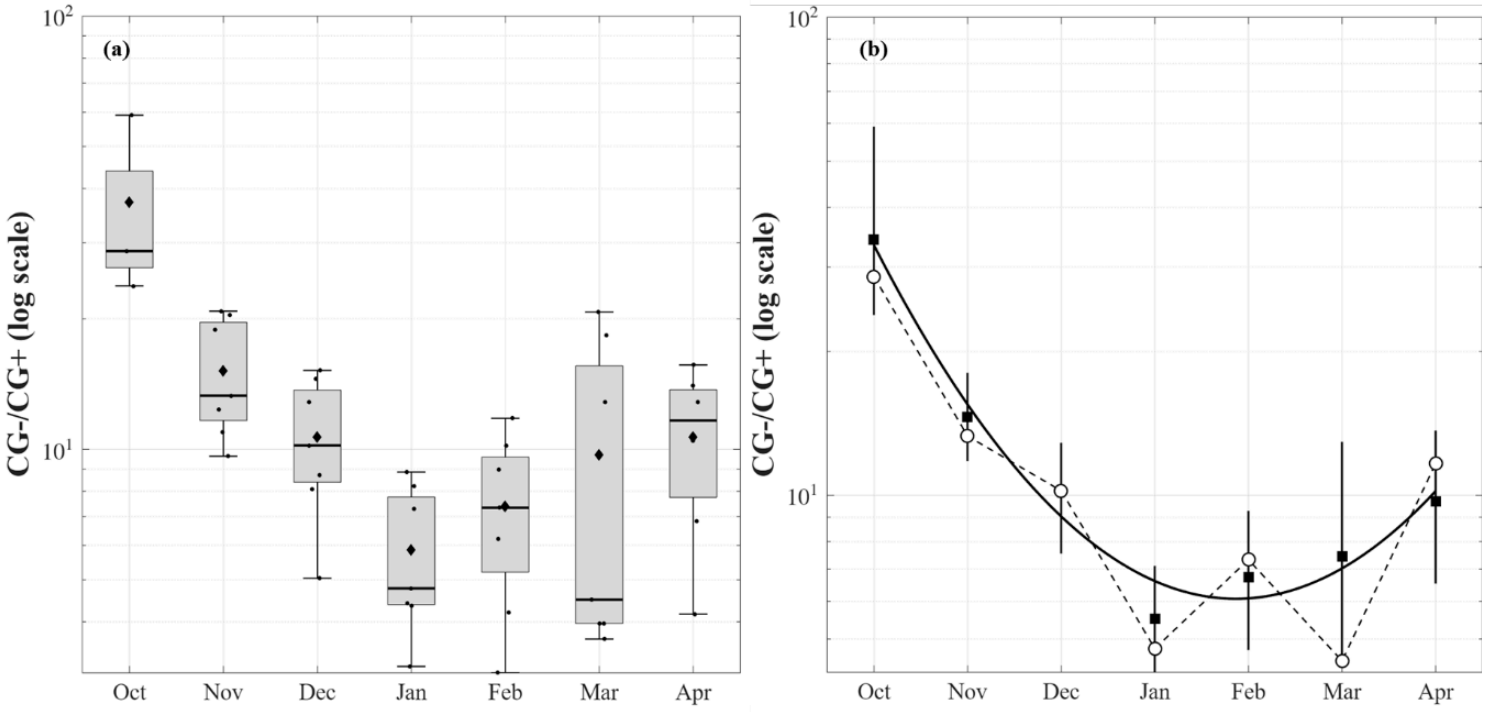


Figure 2

a) Monthly distributions of CG-:CG+ ratios across the winters of 2017–2024. Boxes indicate interquartile ranges, thick horizontal lines denote medians, diamonds indicate means; b) Seasonal evolution of the geometric-mean CG-:CG+ ratio. Squares show geometric means with bootstrap 95% confidence intervals and circles indicate the medians; the solid curve shows a quadratic fit in log space. The minimum occurs near late January-early February.

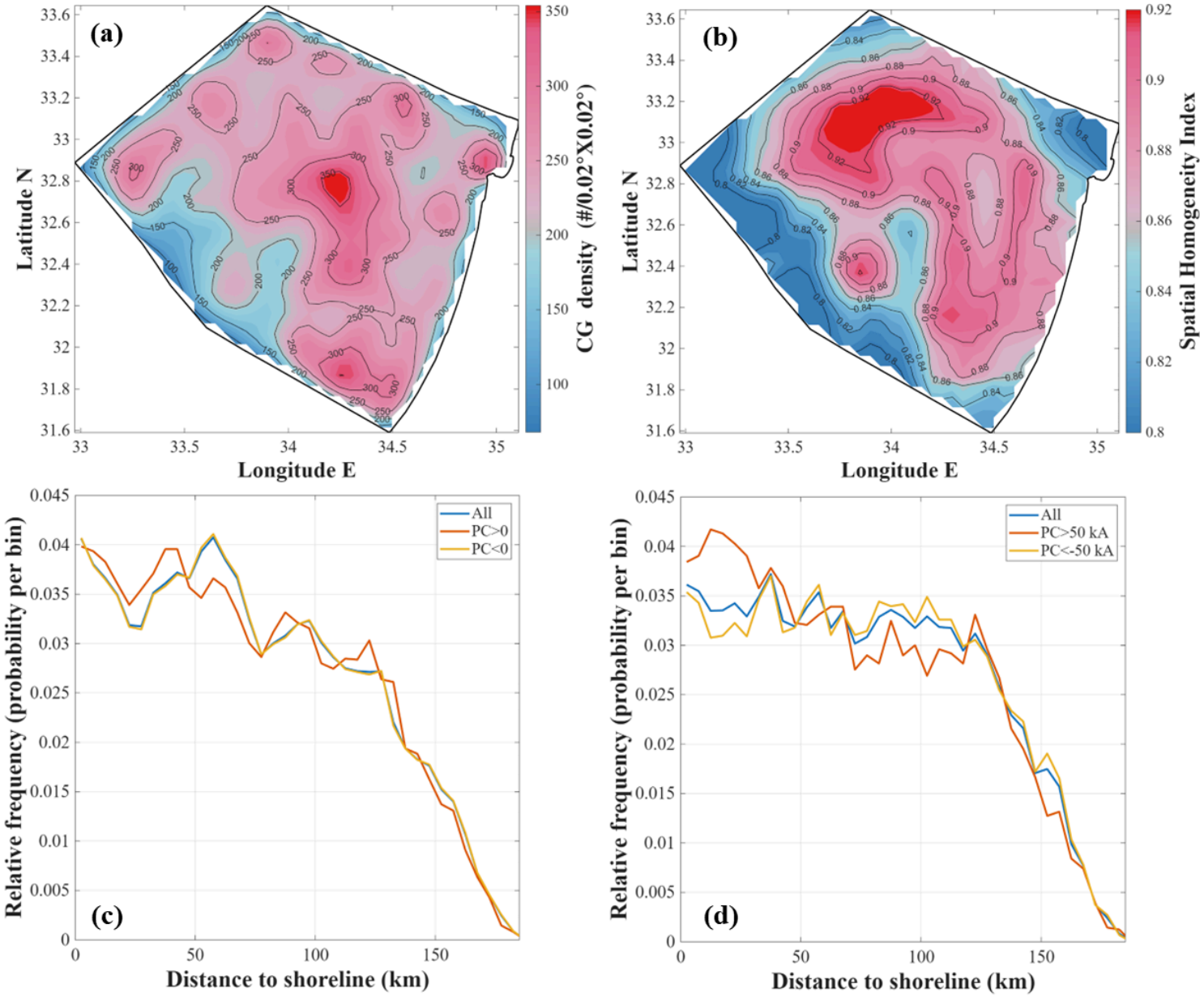


Figure 3

(a) Lightning density in the Israeli Mediterranean IMEEZ during the winter months (October-April) of 2017-2024; (b) Spatial homogeneity index of lightning activity in the IMEE for the same period; (c) Relative frequencies of all CG events in the IMEEZ (blue curve), negative (yellow curve) and positive (orange curve) polarity CG as a function of distance from the shoreline; (d) Relative frequencies of all CG (blue curve), negative (yellow curve) and positive (orange curve) polarity CGs with PCs>|±50| kA as a function of the distance from the shoreline.

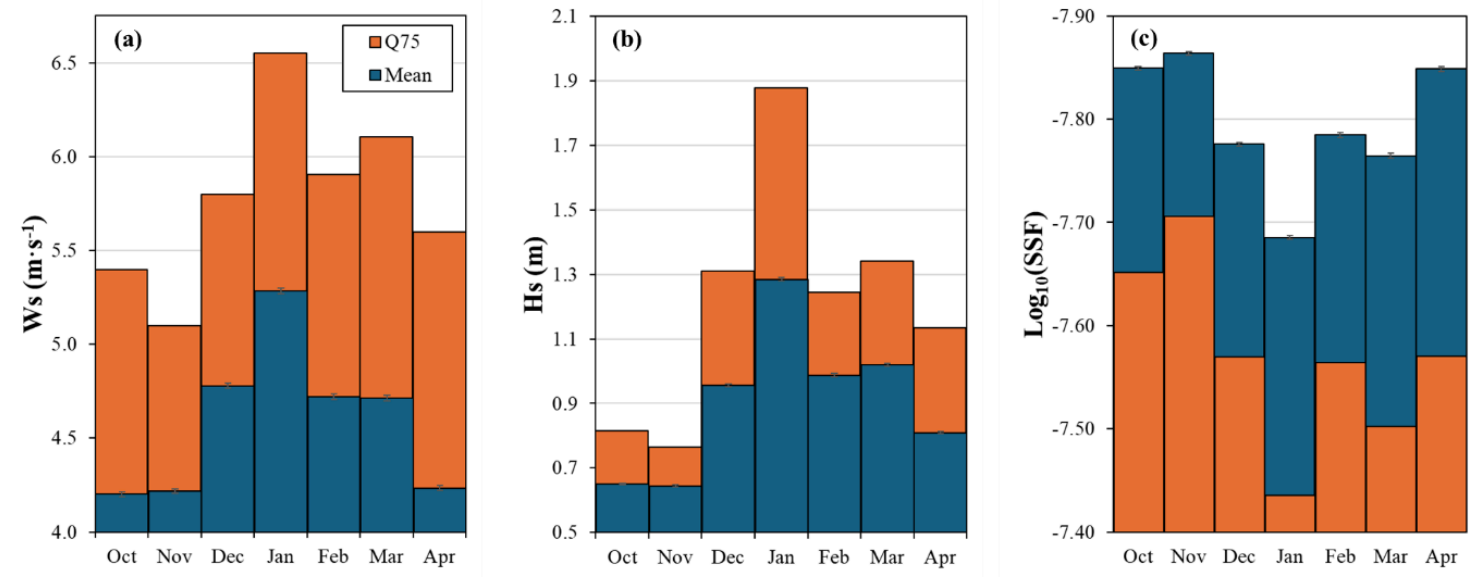


Figure 4

Wintertime storm event segmented monthly mean wind speed (Ws, panel a), significant wave height (Hs, panel b), measured at Hadera, and calculated sea spray flux (SSF, panel c) distributions (blue bars) compared to their fourth quartile values (orange bars) during the period 2017-2024. Note that in panel c, the Y axis is reversed.

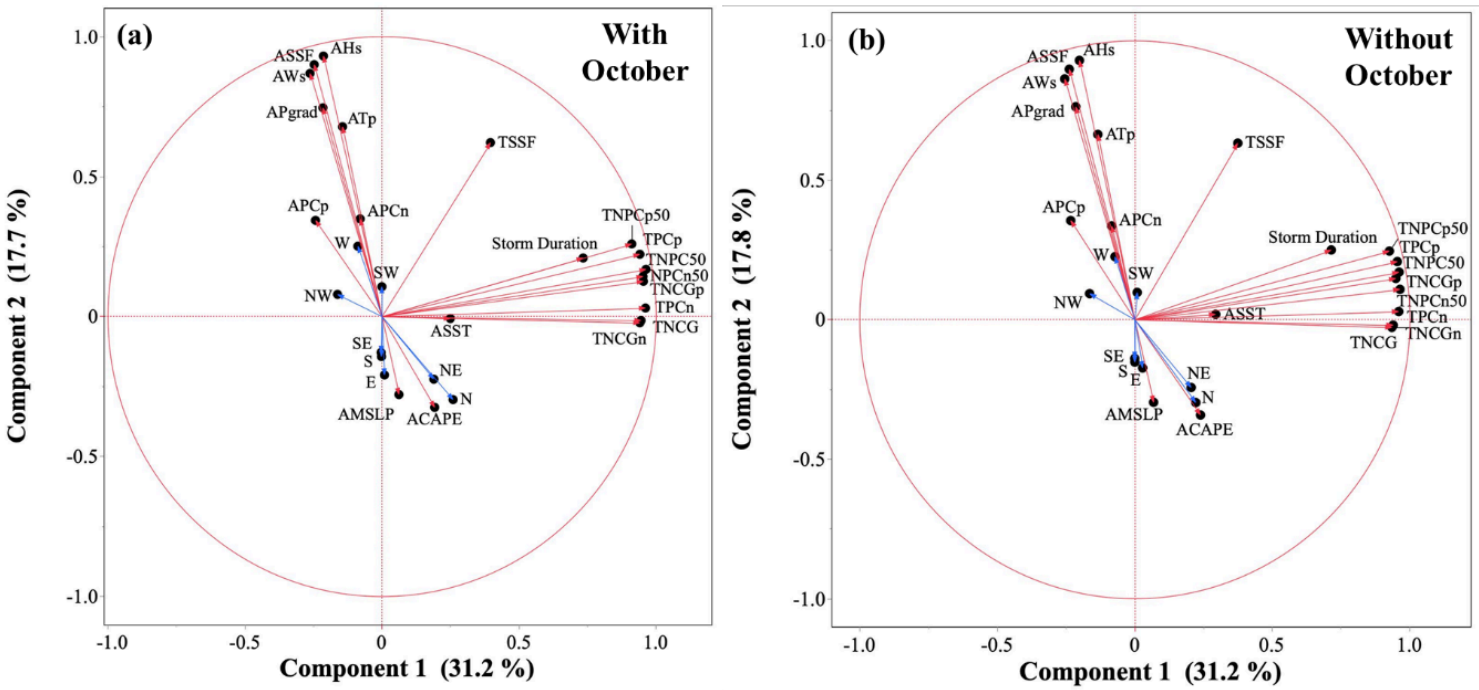


Figure 5

Principal Component Analysis (PCA) biplots for storm-segmented October-April events (2017-2024) in the IMEEZ **(a)**and excluding October **(b)**. The plots show the loadings of lightning metrics and environmental variables. Blue vectors denote storm classes based on mean near-surface wind direction

(N, NE, E, SE, S, SW, W, NW), with vector orientation indicating the typical position of each wind regime in the PCA space. The lightning metrics include: total number of CG events (TNCG); total number of negative and positive polarity CG events (TNCGn and TNCGp, respectively); sum of peak current values for positive and negative polarity CG events (TPCp and TPCn, respectively); average peak current values of negative and positive polarity CG events (APCn and APCp, respectively); total number of both polarities, negative and positive polarity CG events with peak currents >50 kA (TNPC50, TNPCn50 and TNPCp50, respectively); storm duration. The environmental variables include: mean Convective Available Potential Energy (ACAPE); mean Sea Surface Temperature (ASST); mean and total storm event Sea Spray Flux (ASSF and TSSF, respectively); mean wind speed (AWs), significant wave height (AHs) and wave period (ATp); mean surface air pressure (AMSLP) and mean surface pressure gradient (APgrad).

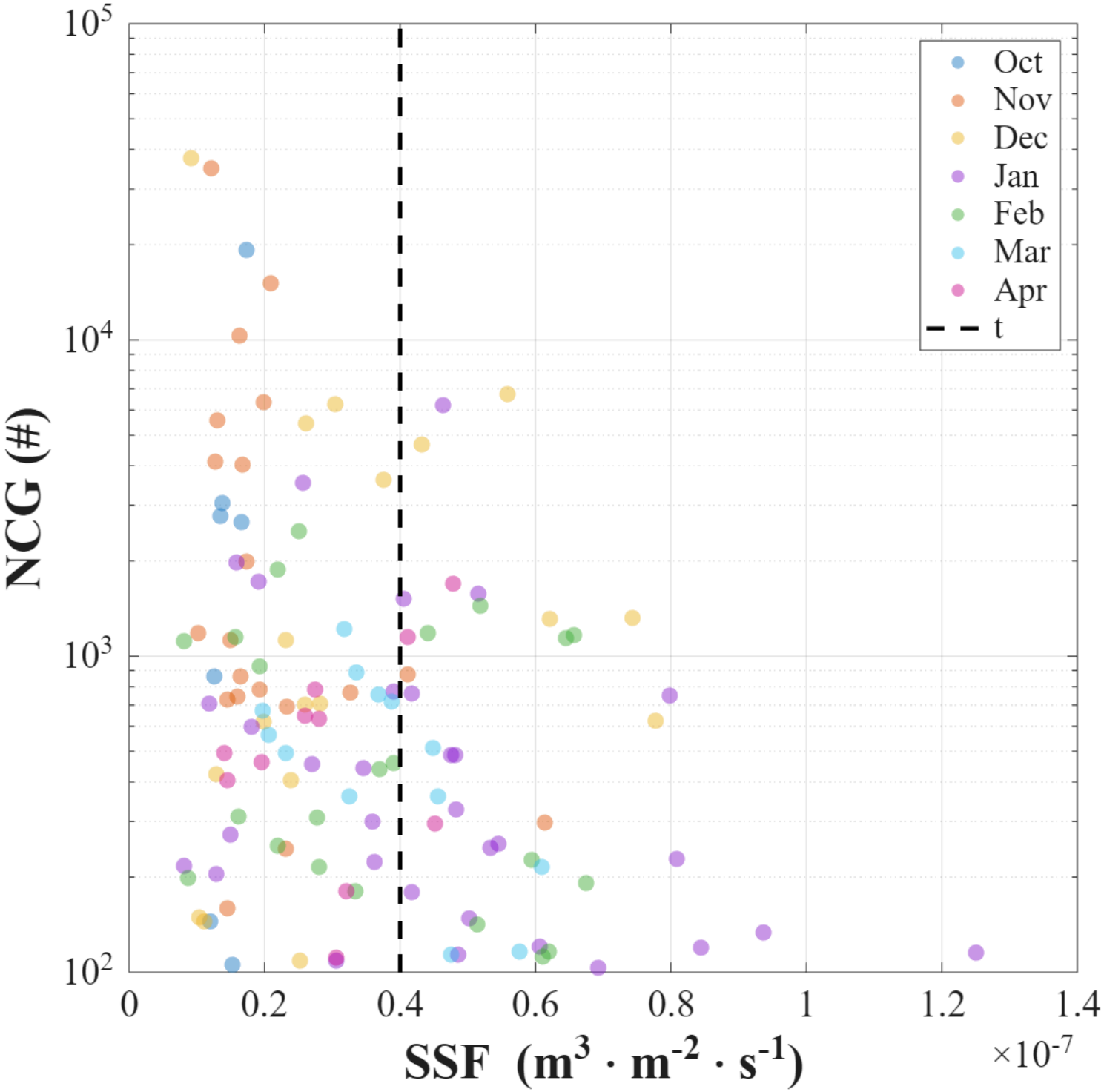


Figure 6

Scatter plot of storm-mean total cloud-to-ground lightning (NCG) versus mean sea-spray flux (SSF) for individual winter storm segments (October–April and NCG<100 excluded). Coloured circles denote their calendar month. The dashed vertical line indicates the visually determined threshold t = $4 \cdot 10^{-8}$ $m^3 \cdot m^{-2} \cdot s^{-1}$.

Supplementary Files

This is a list of supplementary files associated with this preprint. Click to download.

- AsfurandSilvermanSOMTablesandFigures.xlsx